A&A 471, 967–975 (2007)
DOI: 10.1051/0004-6361:20066776

Astronomy & Astrophysics

The structure of sunspot penumbrae

IV. MHS equilibrium for penumbral flux tubes and the origin of dark core penumbral filaments and penumbral grains

J. M. Borrero[1,2]

[1] High Altitude Observatory, NCAR⋆, 3080 Center Green Dr, Boulder 80301, Colorado, USA
e-mail: borrero@ucar.edu
[2] Max Planck Institut für Sonnensystemforschung, Max Plank Strasse 2, 37191 Katlenburg-Lindau, Germany

Received 20 November 2006 / Accepted 17 April 2007

ABSTRACT

Aims. We study the magnetohydrostatic equilibrium of magnetic flux tubes with circular cross sections embedded in a magnetic surrounding atmosphere.
Methods. We solve the static momentum equation in 2.5D to obtain the thermodynamics that are consistent with a prescribed velocity and magnetic fields.
Results. We show that force balance is roughly satisfied if the flux tube's magnetic field is aligned with its axis. Equilibrium is guaranteed if this magnetic field possesses a transverse component. Several forms of this transverse field are investigated. The resulting magnetic field configurations are critically reviewed in terms of the results from spectropolarimetric observations. The thermodynamic structure that allows the flux tube to be in mechanical equilibrium is also calculated. We show that the inferred pressure, density, and temperature stratification reproduce intensity features similar to dark core penumbral filaments and penumbral grains.

Key words. Sun: sunspots – Sun: magnetic fields – Sun: photosphere

1. Introduction

The filamentary structure of sunspot penumbrae is often explained in terms of flux tubes (Bellot Rubio 2003; Solanki 2003; Thomas & Weiss 2004). The equilibrium configuration for such penumbral flux tubes has been studied under the thin-flux tube approximation (Montesinos & Thomas 1997; Schlichenmaier et al. 1998, and references therein). This approximation has the advantage that the governing equations become a set of one-dimensional equations. However, the thin-flux tube approximation has limited applicability in the solar photosphere, since the radius of the penumbral flux tubes is typically comparable to the pressure scale height.

In this case, the problem becomes two-dimensional: density, pressure, and temperature vary over the cross section of the flux tube. Spruit & Scharmer (2006) and Scharmer & Spruit (2006) have suggested that, in this case, homogeneous flux tubes with a circular cross section cannot be in mechanical equilibrium. Such flux tubes are subject to stretching along the vertical direction and flattening along the horizontal direction, which changes their shape and is likely to destroy them.

In this paper we investigate this conjecture and take a first step towards a more realistic modeling of penumbral flux tubes beyond the thin-flux tube approximation. We find analytical solutions for the static momentum equation for horizontal flux tubes with a circular cross section, embedded in a surrounding atmosphere that harbors a potential magnetic field. The basic idea is to set up a generic magnetic and velocity field that satisfies certain conditions: Maxwell equations, boundary conditions, observations, etc. These magnetic field and velocity vectors are brought into the momentum equation. By assuming force balance, we are able to obtain the density and pressure (and therefore temperature) distribution inside the flux tube.

This paper is organized as follows: Sects. 2 and 3 are devoted to describing the basic equations and boundary conditions between the flux tube and the external atmosphere. In Sect. 4 we assume a particular form for the magnetic field in the surrounding atmosphere (potential) and, applying the boundary conditions, we study which configurations are plausible for the flux tube magnetic field. A general form for the flux tube magnetic field is then obtained. In Sect. 5 we apply this general form for the flux tube magnetic field to the static momentum equation, developing a treatment to obtain the thermodynamic structure. Section 6 presents particular cases for the flux tube magnetic field and discusses: a) the general appearance of the magnetic field vector and how it compares with results from spectropolarimetric observations, b) the thermodynamic structure inside the flux tube, c) solutions of the radiative transfer equation in order to simulate the observed continuum intensity emerging from such thermodynamic stratification. In Sect. 7 we critically review our results. Finally, Sect. 8 summarizes the main conclusions of our work.

2. Basic equations and boundary conditions

Let us consider the case of a horizontal flux tube that carries the Evershed flow and is embedded in a static plasma with an inclined magnetic field. The flux tube's cross section is circular with a radius R. For simplicity, its central position in the vertical direction will be taken to be at $z = 0$. The stationary momentum equation can be written (in cgs units) as

$$\rho(\boldsymbol{v}\nabla)\boldsymbol{v} = -\nabla P_{\rm g} + \frac{1}{c}\boldsymbol{j}\times\boldsymbol{B} + \rho\boldsymbol{g} \quad (1)$$

⋆ The National Center for Atmospheric Research (NCAR) is sponsored by the National Science Foundation.

where ρ and $P_{\rm g}$ are the density and gas pressure, and $\boldsymbol{B}$, $\boldsymbol{j}$, $\boldsymbol{v}$ and $\boldsymbol{g}$ are the magnetic field, current, velocity, and gravity vectors, respectively. The gravity is taken as $\boldsymbol{g} = -g\boldsymbol{e}_z$ with $g = 2.74 \times 10^4$ cm s^{-2}. Equation (1) describes the force balance between the inertial force, the pressure gradient, the Lorentz force and the gravity force. Let us use cylindrical coordinates with the axis of symmetry along the tube's axis (x-direction; radial direction along the penumbra). According to Borrero et al. (2004, 2005, 2006a; hereafter referred to as Papers I, II and III), the properties of the flux tubes and the background atmosphere change rather smoothly along the radial direction in the penumbra. These changes are quantitatively smaller than the variations across the plane perpendicular to the tube axis, where large gradients can be present at very small scales. We therefore neglect the variation in any quantity along the x coordinate. This simplifies our problem to a large extent, since now we only consider dependencies on the plane containing the cross section of the flux tube (plane yz; here we can also consider polar coordinates). We can write, separately for the flux tube interior (index "t", tube) and exterior (index "s", surroundings)

$$\boldsymbol{B} = \begin{cases} \boldsymbol{B}_{\rm s} = B_{rs}(r,\theta)\boldsymbol{e}_r + B_{\theta s}(r,\theta)\boldsymbol{e}_\theta + B_{xs}(r,\theta)\boldsymbol{e}_x & r > R \\ \boldsymbol{B}_{\rm t} = B_{rt}(r,\theta)\boldsymbol{e}_r + B_{\theta t}(r,\theta)\boldsymbol{e}_\theta + B_{xt}(r,\theta)\boldsymbol{e}_x & r < R \end{cases} \tag{2}$$

$$\boldsymbol{v} = \begin{array}{ll} \boldsymbol{v}_{\rm s} = 0 & r > R \\ \boldsymbol{v}_{\rm t} = v_{t0}\boldsymbol{e}_x & r < R \end{array} \qquad \rightarrow \text{Evershed flow.} \tag{3}$$

Note that, although there is no dependence on the x-coordinate, the magnetic field configuration is 3-dimensional. The normal component of the external and the internal magnetic fields is assumed to vanish at the tube's boundary $r = R$. This is important in order to keep a clear distinction between the flux tube and the surrounding atmosphere:

$$B^*_{rs} = B^*_{r{\rm t}} = 0 \tag{4}$$

where the superscript * denotes the location of the tube's boundary (R, θ). This boundary condition satisfies the continuity of the normal component of the magnetic field vector across the interface. Substituting our generic magnetic and velocity fields (Eqs. (2) and (3)) into Eq. (1) we obtain,

$$\begin{cases} \boldsymbol{e}_r : 0 = -\frac{\partial P_{\rm g}}{\partial r} + \frac{1}{c}(j_\theta B_x - j_x B_\theta) - \rho g \sin\theta \\ \boldsymbol{e}_\theta : 0 = -\frac{1}{r}\frac{\partial P_{\rm g}}{\partial \theta} + \frac{1}{c}(j_x B_r - j_r B_x) - \rho g \cos\theta. \end{cases} \tag{5}$$

These equations are valid for both the flux tube's exterior and interior. Here $\theta = 0$ lies along $y > 0$ and grows counter-clockwise. We can make use of the relation $\nabla \times \boldsymbol{B} = \frac{4\pi}{c}\boldsymbol{j}$ to obtain

$$\frac{1}{r}\frac{\partial B_x}{\partial \theta} = \frac{4\pi}{c} j_r. \tag{6}$$

3. Pressure and density balance at the boundary

Both the radial components of external and internal magnetic fields vanish in the vicinity of the flux tube's boundary (Eq. (4)). This leads to continuity in the normal stress across the interface (Kippenhahn & Möllenhoff 1975). Therefore, by integrating the Maxwell stress tensor across the flux tube's boundary, we find total pressure balance (thermal plus magnetic) between the flux tube's interior and its surroundings:

$$P^*_{\rm gs} + \frac{B^{2*}_{\rm s}}{8\pi} = P^*_{\rm gt} + \frac{B^{2*}_{\rm t}}{8\pi}. \tag{7}$$

Taking derivatives with respect to θ and regrouping terms, we obtain

$$\frac{\partial P^*_{\rm gs}}{\partial \theta} - \frac{\partial P^*_{\rm gt}}{\partial \theta} = \frac{1}{8\pi}\frac{\partial}{\partial \theta}\left[B^{2*}_{\theta{\rm t}} + B^{2*}_{x{\rm t}} - B^{2*}_{\theta{\rm s}} - B^{2*}_{x{\rm s}}\right]. \tag{8}$$

Terms on the left hand side of Eq. (8) can be written as a function of the density using Eqs. (5) and (6):

$$\begin{aligned} \frac{\partial P^*_{\rm g}}{\partial \theta} &= -\frac{j^*_r B^*_x R}{c} - \rho^* R g \cos\theta \\ &= -\rho^* R g \cos\theta - \frac{1}{8\pi}\frac{\partial B^{2*}_x}{\partial \theta}. \end{aligned} \tag{9}$$

Now, by substituting Eqs. (9) into (8), we obtain

$$\rho^*_{\rm t} - \rho^*_{\rm s} = \frac{1}{8\pi R g \cos\theta}\frac{\partial}{\partial \theta}\left\{B^{2*}_{\theta{\rm t}} - B^{2*}_{\theta{\rm s}}\right\}. \tag{10}$$

Note that Eqs. (7) and (10) link the gas pressure and density of the flux tube and the surrounding atmosphere across the interface. They were obtained with only two assumptions: (a) the radial component of the flux tube and surrounding magnetic field has to vanish at the boundary $r = R$, and (b) velocity and magnetic field vectors are constant in the direction of the tube's axis.

4. Potential external field

Let us consider the case in which the external magnetic field is potential: $\nabla^2\Phi_{\rm s} = 0$ and $\boldsymbol{B}_{\rm s} = -\nabla\Phi_{\rm s}$. This problem can be solved by variable separation. In addition, the boundary conditions given by Eq. (4) must be satisfied:

$$B^*_{sr} = 0. \tag{11}$$

Consider that the external atmosphere is nearly at rest (Papers I, II; see also Bellot Rubio et al. 2004; Bello González et al. 2005) and that it possesses a magnetic field that is somewhat inclined with respect to the vertical z-axis. We therefore assume that $\boldsymbol{B}_{\rm s}$ has the following form far away from the tube:

$$\begin{aligned} \lim_{r\to\infty} \boldsymbol{B}_{\rm s} &= B_0 \cos\gamma_0 \boldsymbol{e}_z + B_0 \sin\gamma_0 \boldsymbol{e}_x = B_0 \cos\gamma_0 \sin\theta \boldsymbol{e}_r \\ &\quad + B_0 \cos\gamma_0 \cos\theta \boldsymbol{e}_\theta + B_0 \sin\gamma_0 \boldsymbol{e}_x, \end{aligned} \tag{12}$$

where B_0 and γ_0 are the strength and inclination (with respect to the vertical to the solar surface) of the external field far away from the flux tube. This yields the following solution for $\boldsymbol{B}_{\rm s}(r,\theta)$:

$$\begin{aligned} \boldsymbol{B}_{\rm s} &= B_0 \sin\gamma_0 \boldsymbol{e}_x + B_0 \sin\theta\cos\gamma_0 \left(1 - \frac{R^2}{r^2}\right)\boldsymbol{e}_r \\ &\quad + B_0 \cos\theta\cos\gamma_0 \left(1 + \frac{R^2}{r^2}\right)\boldsymbol{e}_\theta. \end{aligned} \tag{13}$$

4.1. Uniform internal field

For the flux tube, we now assume that both the magnetic field and Evershed flow are constant and parallel to its axis: $\boldsymbol{B}_{\rm t} = B_{\rm t0}\boldsymbol{e}_x$ and $\boldsymbol{v}_{\rm t} = v_{\rm t0}\boldsymbol{e}_x$. By inserting $\boldsymbol{B}_{\rm t}$ (as well as the external $\boldsymbol{B}_{\rm s}$ given by Eq. (13)) into Eq. (10), we obtain a relation between the external and internal densities of

$$\rho^*_{\rm t} - \rho^*_{\rm s} = \frac{B_0^2 \sin\theta\cos^2\gamma_0}{\pi R g}. \tag{14}$$

Table 1. Parameters of an exponential fit to the vertical stratification of density and gas pressure for two atmospheric models representing the sunspot umbra and quiet Sun[1].

Model	P_0 [dyn cm^{-2}]	H_p [km]	ρ_0 [g cm^{-3}]	H_ρ [km]
Umbra	2.76×10^5	84	1.01×10^{-6}	92
Quiet Sun	1.25×10^5	120	3.18×10^{-7}	130

By adopting the typical values of: $B_0 \simeq 1500$ G, $\gamma_0 \simeq 60°$, $R \simeq 100$ km, we can estimate the density difference across the interface to be

$$\rho_{\rm t}^* \simeq \rho_{\rm s}^* + 7\times10^{-7}\sin\theta \quad \left[{\rm g\,cm^{-3}}\right]. \tag{15}$$

The physical significance of this equation can be understood in terms of the total pressure balance given by Eq. (7) (see also discussion in Borrero et al. 2006b). At the top and bottom of the flux tube, the transverse (azimuthal and radial) component of the external field (Eq. (13)) vanishes: $B_{\theta{\rm s}}(\pm\pi/2, R) = B_{r{\rm s}}(\pm\pi/2, R) = 0$. This creates a pressure imbalance at these points that makes the flux tube expand vertically (z-direction) and flatten horizontally (y-direction). Equation (14) shows that, in order to avoid this effect and keep the flux tube in mechanical equilibrium, the upper portions of the flux tube must be denser than the external atmosphere: $\rho_{\rm t} > \rho_{\rm s}$, such that it becomes antibuoyant. The opposite happens in the lower half of the flux tube: $\rho_{\rm t} < \rho_{\rm s}$. According to Eq. (15), the density difference needed is about 7×10^{-7} g cm^{-3} for typical penumbral conditions.

Another way of looking at the problem is in terms of the pressure scale heights. Considering total pressure balance and assuming that (both inside and outside the flux tube) the gas pressure decays exponentially, it is easy to see that, for a homogeneous field inside the flux tube, the fact that the transverse component of the external field vanishes at the top and bottom of the flux tube, implies a larger pressure scale height inside the flux tube than outside in the lower half of the flux tube, but smaller pressure scale height than the outside in the upper half.

Table 1 shows the parameters of an exponential fit to the vertical density and gas pressure stratification: $\rho(z) \sim \rho_0 \exp -z/H_\rho$, $p(z) \sim P_0 \exp -z/H_p$, for two atmospheric models representing the sunspot umbra (Collados et al. 1994) and the quiet Sun (Borrero & Bellot Rubio 2002). Taking these two models as the limiting cases for the external atmosphere in which the flux tube is embedded, we can take ρ_0 from Table 1 and make $\rho_0 = \rho_{\rm s}^*$. Note that near the umbra, where the density at the continuum level is about $\rho_{\rm s}^* \sim 1\times10^{-6}$ g cm^{-3}, the existence of a flux tube with a uniform magnetic field is plausible.

Indeed, very similar solutions have been presented recently by Schüssler & Vögler (2006) in 3D radiative MHD simulations (see their Fig. 3). In those simulations the intrusion into the external field is caused by a nearly field-free gap, whereas in this situation the flux tube is filled with a horizontal (pointing radially outwards in the penumbra) magnetic field. Note that both situations are equivalent in terms of the density balance presented in Eq. (10).

In the outer penumbra, the right-hand term in Eq. (14) becomes smaller as the external field weakens and becomes more inclined: $B_0 \simeq 1000$ G, $\gamma_0 \simeq 65°$:

$$\rho_{\rm t}^* \simeq \rho_{\rm s}^* + 2\times10^{-7}\sin\theta \quad [{\rm g\,cm^{-3}}]. \tag{16}$$

Here the external density at the continuum level more closely resembles that of the quiet Sun: $\rho_{\rm s}^* \sim 3\times10^{-7}$ g cm^{-3}. On the one hand, the density perturbation (Eqs. (15), (16)) is smaller than the background density. This makes the existence of a flux tube with a homogeneous magnetic field and circular cross section plausible. On the other hand, those two values are very similar. This places the current model at the limit of its validity. There are, however, additional effects that contribute to the equilibrium, such as the subadiabaticity of the external atmosphere (Borrero et al. 2006b), but this only works after the flux tube has already been deformed. Since we are interested in keeping a circular cross section, we will investigate other possibilities. Those could work alone or in combination with a deformed tube embedded in a convectively stable atmosphere.

4.2. Non-uniform internal field

Inspection of Eq. (10) reveals that, if the flux tube magnetic field possesses an azimuthal component, such that

$$\begin{aligned} B_{\theta{\rm t}}^* &= \sqrt{\alpha\mathcal{F}(\theta) + B_{\theta{\rm s}}^{2*}} \\ &= \sqrt{\alpha\mathcal{F}(\theta) + 4B_0^2\cos^2\theta\cos^2\gamma_0}, \end{aligned} \tag{17}$$

then the density difference (Eq. (10)) that follows is

$$\rho_{\rm t}^* - \rho_{\rm s}^* = \frac{\alpha}{8\pi R g}\frac{1}{\cos\theta}\frac{{\rm d}\mathcal{F}(\theta)}{{\rm d}\theta}. \tag{18}$$

We therefore have the freedom to choose α^2 and $\mathcal{F}(\theta)$ in such a way that the right-hand term of Eq. (18) is much smaller than the background density. For instance: $\alpha \ll 8\pi R g \rho_{\rm s}^*$ and $\mathcal{F}(\theta) = \sin\theta$.

Considering now $\nabla \boldsymbol{B}_{\rm t} = 0$, we can write

$$\frac{\partial(rB_{r{\rm t}})}{\partial r} = -\frac{\partial B_{\theta t}}{\partial\theta}. \tag{19}$$

Assuming again separation of variables in the following form

$$B_{r{\rm t}}(r,\theta) = \mathcal{H}(\theta)\mathcal{M}(r) \tag{20}$$

$$B_{\theta{\rm t}}(r,\theta) = \mathcal{G}(\theta)\mathcal{N}(r) \tag{21}$$

with the following boundary conditions, which are used in order to satisfy Eqs. (4) and (17)

$$\mathcal{M}(0) = 0 \qquad \mathcal{M}(R) = 0 \qquad \mathcal{N}(0) = 0 \tag{22}$$

$$\mathcal{N}(R) = 1 \qquad \mathcal{G}(\theta) = \sqrt{\alpha\mathcal{F}(\theta) + 4B_0^2\cos^2\theta\cos^2\gamma_0}. \tag{23}$$

Using Eqs. (19)–(23) and after some algebra, it can be shown that a possible magnetic field configuration is given by

$$\begin{aligned} B_{r{\rm t}}(\theta,r) &= \frac{r}{2R^2}(R-r)\frac{1}{\sqrt{\alpha\mathcal{F}(\theta) + 4B_0^2\cos^2\theta\cos^2\gamma_0}} \\ &\quad\times\left[\alpha\frac{{\rm d}\mathcal{F}(\theta)}{{\rm d}\theta} - 8B_0^2\sin\theta\cos\theta\cos^2\gamma_0\right] \end{aligned} \tag{24}$$

$$B_{\theta{\rm t}}(\theta,r) = \frac{r}{R^2}(3r-2R)\sqrt{\alpha\mathcal{F}(\theta) + 4B_0^2\cos^2\theta\cos^2\gamma_0} \tag{25}$$

$$B_{x{\rm t}} = B_{x{\rm t}0}. \tag{26}$$

Note also that $\boldsymbol{v}_{\rm t}$ is not necessarily parallel to $\boldsymbol{B}_{\rm t}$. This implies that the magnetic field will change in time according to

[2] Note that α has dimensions of Gauss^2, where $\alpha/8\pi$ is equivalent to a magnetic pressure: dyn cm^{-2}.

the induction equation. However, once we consider the magnetic and kinematic properties of our model (Eqs. (3) and (24) through (26)), it turns out that only the diffusive term of the induction equation survives, resulting in magnetic field changes on very long time scales (∼days), which does not affect the discussion presented here.

The only restrictions on the choice of α and $\mathcal{F}(\theta)$ are a) the flux tube transverse magnetic field (given by Eqs. (24) and (25)) must not become singular; b) the total transverse field must be much smaller than the field along the tube's axis: $\sqrt{B_{\theta t}^2 + B_{rt}^2} \ll B_{xt}$ (in order to be consistent with spectropolarimetric observations; see Bellot Rubio et al. 2004); c) ρ_t^* (Eq. (18)) must not become negative (see Sect. 4.1).

5. Thermodynamic structure

Once the magnetic field in our 2-D domain is known (Eq. (13) for the external field and Eqs. (24)–(26) for the flux tube field), we can apply the static momentum equation (Eq. (1); with a velocity field described by Eq. (3)) in order to calculate a density and pressure distribution. For convenience we will work hereafter in Cartesian coordinates.

Since the external field is potential, $\boldsymbol{j} \times \boldsymbol{B} = 0$, Eq. (1) translates into

$$\frac{\partial P_{\rm gs}(z)}{\partial y} = 0 \tag{27}$$

$$\rho_{\rm s}(z) = -\frac{1}{g}\frac{\partial P_{\rm gs}(z)}{\partial z}, \tag{28}$$

Therefore, it is sufficient to prescribe the behavior of the thermodynamic quantities far away from the flux tube ($y \to \infty$). In our case we have adopted a temperature $T_{\rm s}(z)$, density $\rho_{\rm s}(z)$, and gas pressure stratification $P_{\rm gs}(z)$ as given by the cool umbral model of Collados et al. (1994). In order to have a better coverage in deep layers, this model has been extrapolated downwards to 1 Mm with typical solar stratification resulting from 3D numerical simulations (see Cheung 2006; Figs. 3.1 and 3.3).

For the internal (flux tube) atmosphere, we must consider that the magnetic field configuration given by Eqs. (24)–(26) is no longer potential. In particular there is a current oriented along the flux tube axis:

$$\boldsymbol{j}_{\rm t} = j_{xt}\boldsymbol{e}_x = \frac{c}{4\pi r}\left[\frac{\partial}{\partial r}(rB_{\theta t}) - \frac{\partial B_{rt}}{\partial \theta}\right]\boldsymbol{e}_x. \tag{29}$$

In this case, considering the horizontal (y-axis) direction of static momentum equation (Eq. (5)) yields the pressure distribution inside the flux tube:

$$P_{\rm gt}(y,z) = -\frac{1}{c}\int j_{xt}B_{zt}{\rm d}y + C(z), \tag{30}$$

where B_{zt} is obtained from Eqs. (24), (25) and j_{xt} from Eq. (29). The integration constant $C(z)$ can be evaluated by imposing total pressure balance at the flux tube boundary.

$$P_{\rm gt}\left(\pm\sqrt{R^2-z^2}, z\right) = P_{\rm gs}(z) + \frac{B_0^2\sin^2\gamma_0 - B_{xt0}^2 - \alpha\mathcal{F}(\theta)}{8\pi}. \tag{31}$$

Once the pressure is known for every point inside the flux tube, the vertical component of the momentum equation yields the density:

$$\rho_{\rm t}(y,z) = \frac{1}{g}\left[\frac{j_{xt}B_{yt}}{c} - \frac{\partial P_{\rm gt}}{\partial z}\right]. \tag{32}$$

Given the analytical solution for the magnetic field, Eqs. (24)–(26), the gas pressure and density also have analytical expressions that can be evaluated through Eqs. (30)–(32). These solutions ensure that there is no net force acting on the flux tube and it is therefore in mechanical equilibrium. Note that the term involving the velocity field (advection term) in Eq. (1) vanishes as long as we assume that the velocity is concentrated inside the flux tube and that it is parallel to its axis (x-axis; Eq. (3)). Once we have two-dimensional (yz) maps of the density and gas pressure, the temperature can be evaluated using the ideal gas equation. A variable mean molecular weight is used in order to account for the partial ionization of the different atomic species.

6. Results

6.1. Magnetic field

The first example we will consider is $\alpha = 0$. This case is particularly interesting because it is valid for any $\mathcal{F}(\theta)$. In this case, the magnetic field is

$$\begin{aligned}\boldsymbol{B}_{\rm s} &= B_0\sin\gamma_0\boldsymbol{e}_x + B_0\sin\theta\cos\gamma_0\left(1-\frac{R^2}{r^2}\right)\boldsymbol{e}_r \\ &\quad + B_0\cos\theta\cos\gamma_0\left(1+\frac{R^2}{r^2}\right)\boldsymbol{e}_\theta\end{aligned} \tag{33}$$

$$\begin{aligned}\boldsymbol{B}_{\rm t} &= B_{xt0}\boldsymbol{e}_x - \frac{2r}{R^2}(R-r)B_0\sin\theta\cos\gamma_0\boldsymbol{e}_r \\ &\quad + \frac{2r}{R^2}(3r-2R)B_0\cos\theta\cos\gamma_0\boldsymbol{e}_\theta.\end{aligned} \tag{34}$$

Figure 1 shows the total magnetic field (top panel) and inclination with respect to the vertical (middle panel) resulting from Eqs. (33) and (34) with the following parameters: $B_0 = 1700$ Gauss, $\gamma_0 = 65°$, $B_{xt0} = 1200$ Gauss, $R = 125$ km. The inclination with respect to the vertical (z-axis) direction is defined as $\gamma = \cos^{-1}(B_z/B)$. The bottom panel in Fig. 1 displays the field lines for the transverse field (yz plane). Inside the flux tube, the magnetic field is mainly align with the x-axis $B_{xt} \gg \sqrt{B_{\theta t}^2 + B_{rt}^2}$, but points slightly upwards along the sides ($\gamma \sim 80°$) and downwards in its center: $\gamma \sim 100°$.

In spite of the simplicity of this model, the overall configuration displays many similarities with recent investigations of the penumbral fine structure. For instance, (a) at a height corresponding to the axis of the flux tube, the internal (flux tube) magnetic field is weaker than the external (surrounding field) by an average amount of 600 Gauss (Papers I–III; see also Bellot Rubio et al. 2004); (b) the average flux tube magnetic field is mostly horizontal $\gamma \sim 90°$, while the external field is inclined (next to the flux tube) about 50° with respect to the vertical; (c) an observer at disk center could see an inclination for the magnetic field inside the flux tube that is larger than 90° despite the fact that the flux tube axis is perpendicular to the observer. This is due to the transverse field inside the flux tube having a negative component $B_z < 0$ in its inner part (see Fig. 1 bottom panel). The existence of magnetic flux returning into the solar photosphere has appeared in many different works (see, e.g. Westendorp Plaza et al. 1997; del Toro Iniesta et al. 2001; Schlichenmaier et al. 2004). In the present model, returning flux can be explained either by a flux tube pointing downwards or, even if its axis is aligned with the x-axis (as in Fig. 1), as a consequence of the transverse field lines B_{rt} and $B_{\theta t}$.

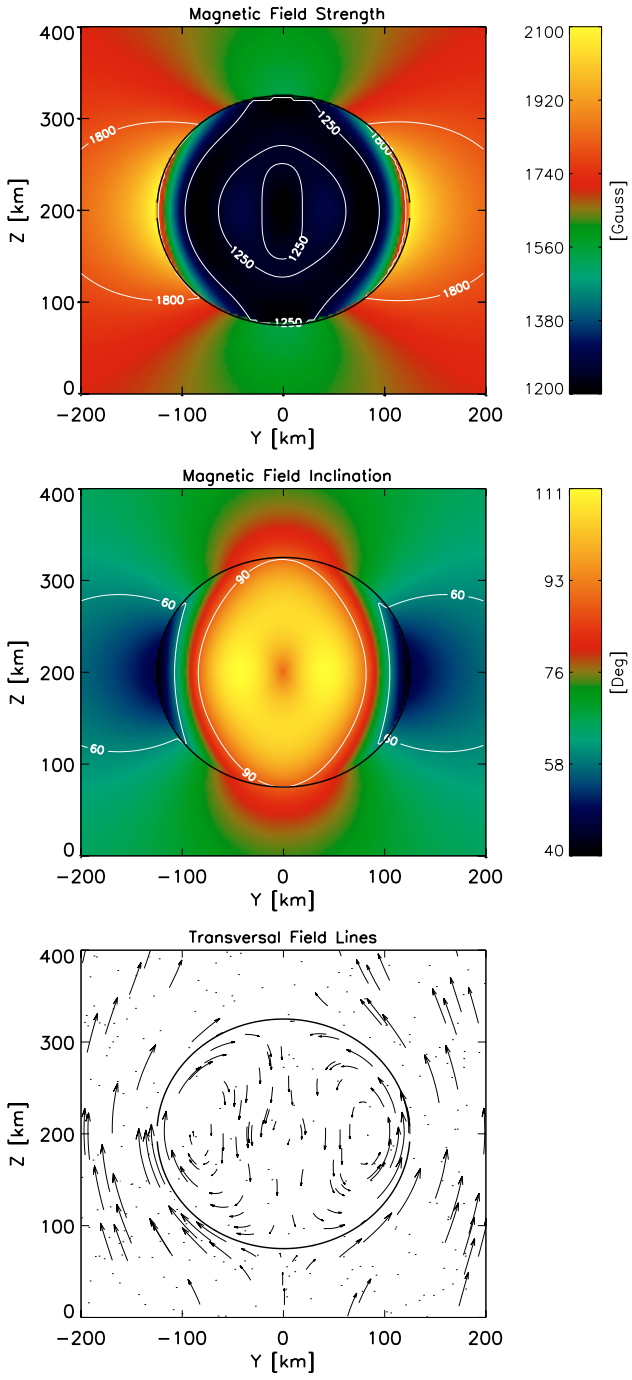

Fig. 1. Color plots of the total magnetic field strength (*top panel*) and magnetic field inclination (*middle*) for the following parameters: B_0 = 1700 Gauss, $\gamma_0 = 65°$, B_{xt0} = 1200 Gauss, R = 125 km. Note that the strength of the magnetic field inside the flux tube along its axis is B_{xt0} = 1200 Gauss, therefore almost all the magnetic field seen inside the flux tube goes along the x axis. The *bottom panel* displays the direction of the transverse field.

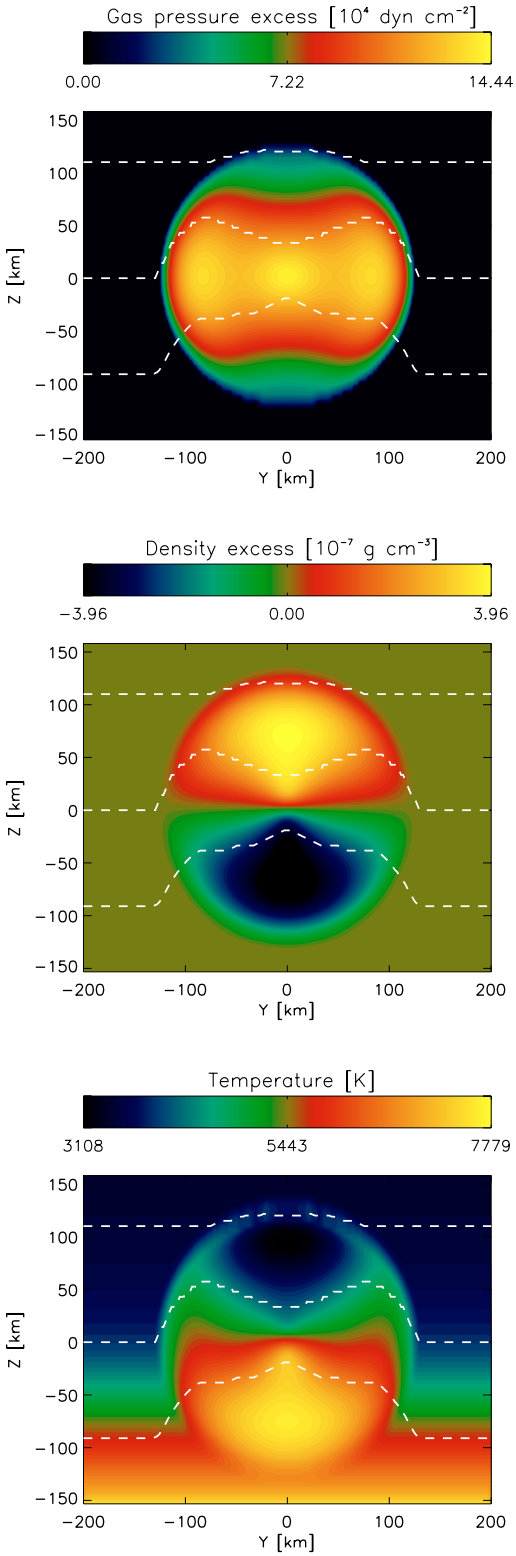

Fig. 2. *Top panel*: gas pressure excess $P_g(y,z) - P_{gs}(\infty,z)$. *Middle panel*: same for density excess $\rho_g(y,z) - \rho_{gs}(\infty,z)$. *Bottom panel*: temperature distribution $T(y,z)$. Dashed yellow lines indicate (from lowermost to uppermost) the τ_5 = 10, 1, 0.1 levels.

6.2. Thermodynamic structure

Figure 2 (top and middle panels) shows surface plots of the density and gas pressure excess (with respect to the surrounding at each height) as obtained from the same magnetic field configuration as in Fig. 1. This distribution ensures that the flux tube is in mechanical equilibrium. The vertical scale z has been shifted so that the the continuum τ_5 = 1 level (denoted by the middle white dashed line) in the surrounding atmosphere lies at z = 0. The center of the flux tube is located at z_0 = 0 km (same height as the continuum level in the surrounding atmosphere). In this figure $P_{gs}(\infty,z)$ and $\rho_{gs}(\infty,z)$ decay exponentially with height z.

As in Sect. 4.1, the upper part of the flux tube is denser than the surroundings at the same height, while the opposite happens in the lower part of the flux tube. This effect follows from the requirement of total pressure balance at the top and bottom of the flux tube. In addition, according to Eq. (18), there is no density change across the boundary between the flux tube and the magnetic surrounding: $\rho_s^* = \rho_t^*$.

The temperature distribution is presented in Fig. 2 (bottom panel). Note that the combination of low density and high gas pressure in the lower portions of the flux tube yields high temperatures in this region. In addition, the high densities found in the upper half of the flux tube result in low temperatures there. Depending upon the choice of our model parameters B_0, γ_0, B_{xt0}, z_0, and R, sometimes unrealistically high/low temperatures (in the lower/upper half) may result. The evolution of any hot plasma element, which rises adiabatically with typical entropy values corresponding to the bottom of the convection zone, limits the temperature at the photosphere to roughly $T_{\max} < 13\,500$ K. Although we are not aware of a lower limit for the temperature, we also consider that any value below 2000 K is not realistic.

Figure 3 presents a parameter study aiming at identifying the regions where the resulting temperatures are within the allowed range ($T_{\max} < 13\,500$ and $T_{\min} > 2000$) K. Since we have 5 model parameters, we kept three of them fixed while varying the other two: B_0 and B_{xt0} (top panel), R and γ_0 (middle panel), and finally R and z_0 (bottom panel). In these plots, the solid lines separate the regions where $T_{\max}$ and $T_{\min}$ are below/above 13 500 K and 2000 K, respectively. The shaded areas are the regions where both constraints are met. Figure 3 shows that, for very strong fields ($B_0 > 1800$ and $B_{xt0} > 1600$ G), it is difficult to satisfy the constraint of $T_{\max} < 13\,500$ K. The same happens for very vertical external magnetic fields ($\gamma_0 < 60^\circ$) and for thin flux tubes ($R < 50$ km). However, this does not mean that the model presented here is not valid near the umbra. Indeed, Fig. 1 shows a magnetic field configuration that resembles that region very closely.

We also repeated the calculation of Fig. 3 but using the mean penumbral model of del Toro Iniesta et al. (1994) as a background atmosphere. This model is similar (in its density and pressure stratification) to a quiet Sun model. Our results indicate that temperatures below 13 500 K are obtained for B_0 and $B_{xt0} \lesssim 1200$ Gauss and $R > 100$ km. This is consistent with our discussion in Sect. 4.1.

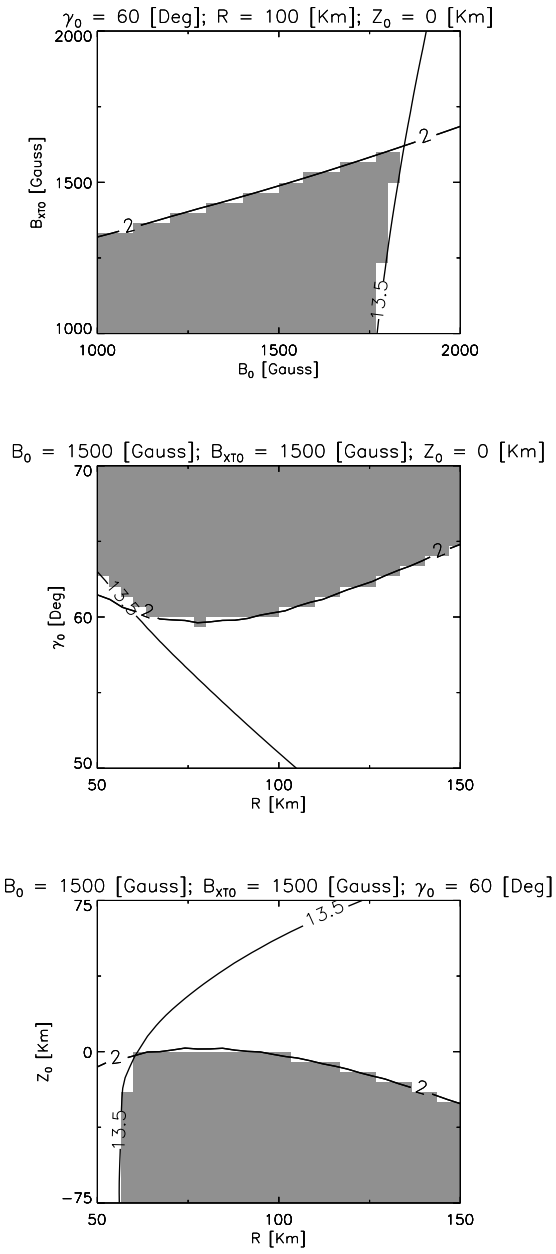

Fig. 3. Shaded areas indicate the range for which the model parameters results in minimum temperatures (inside the flux tube) higher than 2000 K and maximum temperatures lower than 13 500 K. Only two parameters are allowed to change at a time: B_{xt0} and B_0 (*top panel*), γ_0 and R (*middle panel*), z_0 and R (*bottom panel*).

6.3. Emergent intensity: dark core penumbral filaments and penumbral grains

High-resolution observations of individual penumbral filaments in the G-band and continuum intensity at 4877 Å (Scharmer et al. 2002; Rouppe van der Voort et al. 2004; Sütterlin et al. 2004) show intensity enhancements at the edges of the filament. This is accompanied by a drop in the core intensity (Fig. 2 and Fig. 3 in Scharmer et al. 2002). The contrast varies from image to image but in general it is higher in the G-band images than at 4877 Å. Ever since this discovery, this particular feature has been referred to as *dark core penumbral filaments*. Other penumbral features reveal *penumbral grains* composed of what looks like three different kernels next to each other (Fig. 6 in Rouppe van der Voort et al. 2004).

We employed a numerical code to solve the Radiative transfer equation (Frutiger 2000) and to compute the values of the observed continuum intensity (at a reference wavelength of 5000 Å) for each ray path along the z-direction. This returns the continuum intensity as a function of the position y across the filament. The result is convolved with an Airy function with an *FWHM* of 100 km in order to account for the limited spatial resolution of the observations.

We did three different experiments, in which continuum images at a reference wavelength of 5000 Å are produced by varying different model parameters one at a time. Results are presented in Fig. 4: varying z_0 (top panel), R (middle panel), and γ_0 (bottom panel). The values for the other parameters are indicated in the corresponding figures.

In the first experiment (Fig. 4; top panel), the only parameter that changes is z_0 (central position of the flux tube with respect to the $\tau = 1$ level of the background atmosphere). The intensity

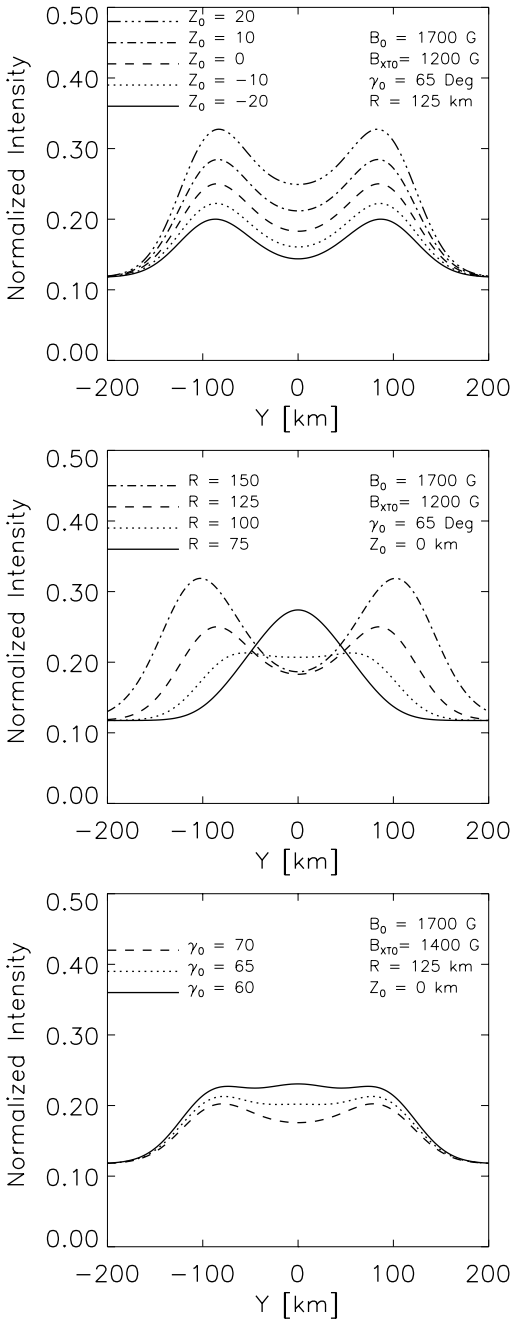

Fig. 4. Variation in the observed continuum intensity at a reference wavelength of 5000 Å along the cross section of the flux tube. *Top panel*: all parameters are kept constant (see text for details) except for the position of the flux tube axis with respect the continuum level in the external atmosphere: z_0. *Middle panel*: same as before but now the radius of the flux tube is the only parameter that changes. *Bottom panel*: same as before but now what varies is the inclination of the external field γ_0.

pattern that results is very similar to a *dark core penumbral filament*. The intensity contrast between the background and the bright feature is stronger the higher the flux tube is located. Note that the background intensity is about 0.12 units of the quiet Sun intensity, resulting from the use of the cool umbral model by Collados et al. (1994).

For the second test (Fig. 4; middle panel), we fix $z_0 = 0$ while the flux tube radius R changed from 75 to 150 km. For small flux-tube radii, we obtained an intensity pattern that would be

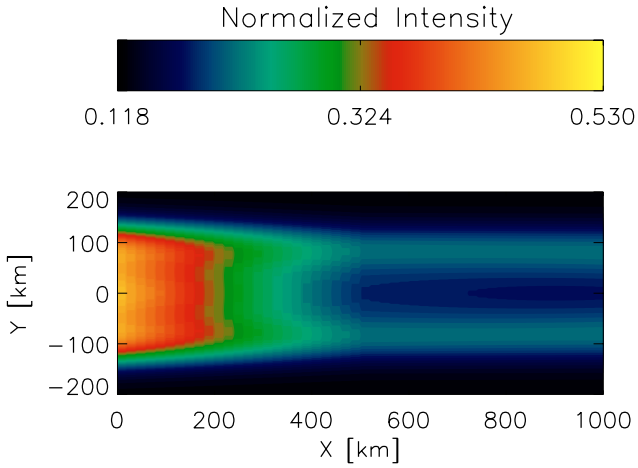

Fig. 5. Simulated intensity map of a penumbral filament. γ_0 and z_0 change (along the x-direction) from 60° to 70° and from 50 to 0 km. The remaining parameters are: B_0 = 1700 Gauss, B_{tx0} = 1300 Gauss, and R = 125 km.

identified with a *penumbral grain*. With increasing diameter, the emergent intensity morphology shifts to that of a *dark core filament*. In the third test we explored the effects of a varying inclination for the external field: γ_0 (see Fig. 4; bottom panel). In this example, more vertical external fields yield *penumbral grains*. When γ_0 increases, the intensity at the center of the flux tube decreases and we start to see a *dark core filament*. These are just examples of the kind of intensity features that the model is able to produce. In all examples we were careful to select only a set of parameters that keep the minimum/maximum temperatures inside the flux tube above/below 2000/13 500 K, respectively.

Inversions of spectropolarimetric observations (Papers I–III; Bellot Rubio et al. 2004; Rüedi et al. 1998, 1999) indicate that flux tubes are located high above the continuum formation height in the inner penumbra, but they are found near to it in the outer penumbra[3]. In addition, the external field becomes more horizontal as we move away from the umbra. Furthermore, although not entirely clearly based on the interpretation of the net circular polarization (NCP), it appears that the radius of the flux tube increases radially in the penumbra[4] (x-direction). To test what kind of radial feature would be obtained under these assumptions, we produced 50 different continuum images where the flux tube is initially (inner penumbra) located at $z_0 = 50$ but descended linearly down to $z_0 = 0$ in the last image (farther from the umbra). At the same time, the inclination of the external field changed linearly from 60° in the first image to 70° in the last one. The radius, R, was kept constant at 125 km, however. Results are presented in Fig. 5, where the similarities with observed features in high-resolution continuum images (see, e.g. Fig. 5 in Rouppe van der Voort et al. 2004) are remarkable.

Note that for this test we assumed that some physical parameters depend on the x coordinate. This has no particular consequence on our main assumptions, as long as the changes along the radial direction in the penumbra are small (see Sect. 2).

[3] A common interpretation of this result is that the flux tube is located at a fairly constant height. However, the height separation between the flux tube and the external $\tau = 1$ level decreases away from the umbra as the Wilson depression is reduced.

[4] Magnetic flux conservation, together with a decreasing magnetic field strength inside the flux tube as a function of x, leads to a radially increasing flux tube radius.

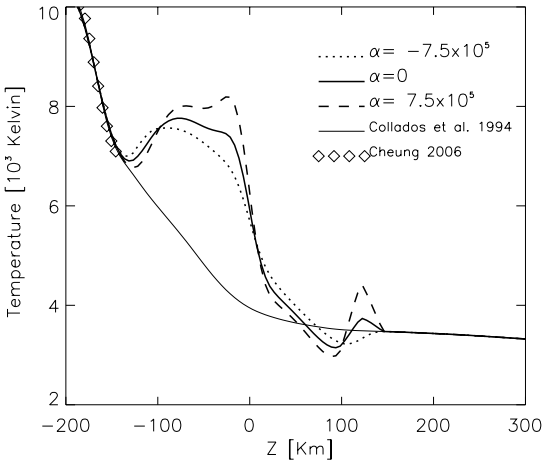

Fig. 6. Vertical stratification of the temperature along the center of the flux tube: $T(0, z)$ for different values of α. Dotted line: $\alpha = -7.5 \times 10^5$; solid line: $\alpha = 0$; dashed line: $\alpha = 7.5 \times 10^5$. For this example we have adopted: $B_0 = 1700$ Gauss, $B_{xt0} = 1200$ Gauss, $\gamma_0 = 65°$, $R = 125$ km, $Z_0 = 0$ km. Note that $\alpha < 0$ produces a smoother temperature stratification, with lower maximum temperatures. The solid thin line corresponds to the surrounding umbral atmosphere (Collados et al. (1994). Diamonds represent the extrapolation towards deep layers starting at $z \sim -150$ km (see Sect. 5).

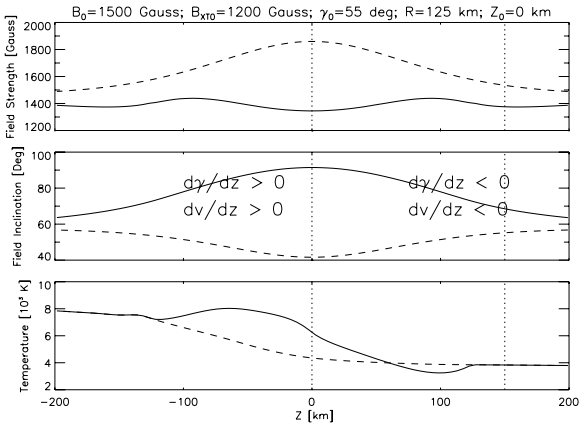

Fig. 7. Example of the average properties for the flux tube (solid) and surrounding atmosphere (dashed). From top to bottom: magnetic field strength, magnetic field inclination, and temperature. Note the discrepancies and similarities with the model for embedded flux tubes used in Borrero et al. (2005; Fig. 4). In the middle panel we indicate the sign of $\mathrm{d}\gamma/\mathrm{d}z$ and $\mathrm{d}v/\mathrm{d}z$. The sign of the velocity gradient is calculated using Eq. (3): the flux tube carries the Evershed flow, whereas the surrounding is at rest.

6.4. Results for $\alpha \neq 0$

For $\alpha \neq 0$, functions such as $\mathcal{F}(\theta) = \sin\theta$ or $\mathcal{F}(\theta) = \cos\theta$ lead to singular $B_{rt}(r, \theta)$ functions (see Eq. 24). However, $\mathcal{F}(\theta) = \cos^2\theta$, $\mathcal{F}(\theta) = \sin^2\theta$ and $\mathcal{F}(\theta) = 1$ are all plausible.

We repeated all the calculations presented in Sect. 6 for the case $\alpha \neq 0$ and $\mathcal{F}(\theta) = \cos^2\theta$. In this case, α is constrained between $\simeq[-10^6, 10^6]$ to avoid singularity problems in Eq. (24) and large density perturbations in Eq. (18). Results show that the maximum temperature inside the flux tube increases for $\alpha > 0$, but the opposite occurs for $\alpha < 0$ (see Fig. 6). This expands the allowed ranges in Fig. 3 for $\alpha < 0$ as compared to $\alpha = 0$, and vice-versa for $\alpha > 0$.

7. Critical comparison with observations

Although the main intent of this paper is to describe equilibrium solutions of a horizontal flux tube embedded in a magnetic surrounding atmosphere, it is unavoidable to make comparisons between the model predictions and observations. In previous sections we have mentioned cases where that comparison is positive. In this section we turn our attention to aspects where our model faces difficulties.

7.1. Vertical gradients in the field inclination

In order to reproduce the NCP observed in sunspots, strong vertical gradients in the field inclination (about 40° in about 100 km: Sánchez Almeida & Lites 1992) are required. In papers II and III, we used a *simple* (the flux tube cross section was assumed to be square) flux tube model where those large gradients in the inclination were produced at the lower and upper tube boundaries. In this manner, we successfully reproduced the observed NCP and the full polarization profiles (see also Schlichenmaier et al. 2002; Müller et al. 2002 and Müller et al. 2006).

A closer look at *more realistic* (circular cross section) flux-tube models highlights a lack of adequate vertical gradients: see Fig. 10. Since $B_z = 0$ on top of the flux tube, the inclination of the external field there is still 90°. A 40° change in the inclination along the vertical direction can only be attained if we compare the field inclination inside the flux tube with the external one 150 km above the upper boundary (compare two vertical dotted lines in Fig. 10; middle panel). However, at this point we start moving outside the region in which the spectral lines are formed.

A possible solution to the problem is to reduce the radius of the flux tube. In this case there would be enough vertical length to accommodate the flux tube and at the same time to let the external field spread upwards long enough to see significant changes in the field inclination. A second possibility is to relax the hypothesis of circular cross sections. A boundary layer with a cusp shape (Schüssler & Vögler 2006; Scharmer & Spruit 2006) allows $B_z > 0$ on top of the flux tube. This of course makes the external field more vertical there and increases the $\Delta\gamma$ across the upper boundary.

7.2. Lower flux-tube boundary

Perhaps the most serious problem that our model faces is the location of the lower boundary of the flux tube. According to our calculations and examples shown here (see Figs. 2 and 6), the $\tau_5 = 1$ level is always formed inside the flux tube. This is a consequence of the high temperatures and large opacities present in the lower half of the flux tube. If our model is correct, this would indicate that the lower boundary of the flux tube would be invisible to spectropolarimetric observations. However, such observations seem to indicate (Fig. 7 in Borrero et al. 2005; see also Fig. 6 in Borrero et al. 2006a) that the lower boundary is visible.

Furthermore, the impossibility of observing the flux tube lower boundary would make it difficult to explain (without calling upon horizontal gradients) the observed change in the sign of $\mathrm{d}\gamma/\mathrm{d}z$ and $\mathrm{d}v/\mathrm{d}z$ throughout the penumbra (see Fig. 5 in Borrero et al. 2004). Indeed, this observational result is what led Bellot Rubio et al. (2002) and Mathew et al. (2003) to first postulate the existence of flux tubes with two defined boundaries. Let us keep in mind that, in the flux tube model (Fig. 10; middle panel), we

have $d\gamma/dz > 0$ and $dv/dz > 0$ in the lower half of the flux tube, but $d\gamma/dz < 0$ and $dv/dz < 0$ in the upper half. It appears now that realistic flux tube models have the region where $d\gamma/dz > 0$ and $dv/dz > 0$ beyond the line-forming region.

8. Conclusions

We have studied the equilibrium of horizontal magnetic flux tubes (with circular cross sections) embedded in an external atmosphere with a more vertical magnetic field (assumed to be potential). Our study differs from previous investigations in that the flux tubes are not necessarily *thin*. We have found that, for typical penumbral conditions, the equilibrium condition is hardly satisfied if the flux-tube's magnetic field is aligned with its axis. This situation is alleviated if the tube's magnetic field possesses a transverse component.

We have obtained the thermodynamical configuration resulting from different possibilities for the transverse magnetic field inside the flux tube. We have found that the thermodynamical structure of such flux tubes reproduces the dark core penumbral filaments and penumbral grains observed at high spatial resolution. This happens as a consequence of the high densities and low temperatures found on the upper part of the flux tube (right above the continuum $\tau = 1$ level formation height).

The overall magnetic configuration explains many (but not all, see Sect. 7), results from spectropolarimetric observations of sunspot penumbrae. It also explains recent observations that find the Evershed effect mainly concentrated in the dark lanes of penumbral filaments (Bellot Rubio et al. 2005; Rimmele & Marino 2006; Langhans et al. 2007). Our Fig. 2 shows that the Evershed effect appears predominantly at the flux tube's core. This is due to a higher opacity at the tube's center (where the dark core originates) as compared to its sides. Our model also predicts that, although weaker, flows should also appear on the brights sides on the filaments. This agrees with the findings of Bellot Rubio et al. (2005).

Questions, such as the stability and temporal evolution of the proposed configurations, are beyond the scope of this work and need to be addressed by other means. In particular our approach neglects the energy equation. It is also important to note that the presence of a high density plasma region immediately above a low-density region makes the model prone to Rayleigh-Taylor instabilities. It is unclear how the horizontal field inside the flux tube might help to stabilize the system (Jun et al. 1995).

Acknowledgements. Sami Solanki, Manfred Schüssler, Matthias Rempel, Luis Bellot, Rolf Schlichenmaier, and Goran Scharmer are gratefully acknowledged for continuous and stimulating discussions on the topic. Our thanks go to Hector Socas-Navarro for carefully reading the manuscript. This work was completed during a visit to Katlenburg-Lindau with the financial support and sponsorship of the Max Planck Institut für Sonnensystemforschung. This research has made use of NASA's Astrophysics Data System.

References

Bello González, N., Okunev, O. V., Domínguez Cerdeña, I., Kneer, F., & Puschmann, K. G. 2005, A&A, 434, 317
Bellot Rubio, L. R. 2003, in Proceedings of the Solar Polarization Workshop 3, ed. J. Trujillo-Bueno, & J. Sánchez Almeida, ASP Conf. Ser., 307, 301
Bellot Rubio, L. R., Collados, M., Ruiz Cobo, B., et al. 2002, Il Nuovo Cimento C, 25, 543
Bellot Rubio, L. R., Balthasar, H., & Collados, M. 2004, A&A, 427, 319
Bellot Rubio, L. R., Langhans, K., & Schlichenmaier, R. 2005, A&A, 443, L7
Borrero, J. M., & Bellot Rubio, L. R. 2002, A&A, 385, 1056
Borrero, J. M., Solanki, S. K., Bellot Rubio, L. R., Lagg, A., & Mathew, S. K. 2004, A&A, 422, 1093, Paper I
Borrero, J. M., Lagg, A., Solanki, S. K., & Collados, M. 2005, A&A, 436, 333, Paper II
Borrero, J. M., Solanki, S. K., Lagg, A., Socas-Navarro, H., & Lites, B. 2006a, A&A, 450, 383, Paper III
Borrero, J. M., Rempel, M., & Solanki, S. K. 2006b in Proceedings of the Solar Polarization 4, ed. R. Casini, & B. Lites, ASP Conf. Ser., 358, 19
Cheung, M., Ph.D. Thesis (2006) University of Göttingen (Germany) (Copernicus GmbH)
Collados, M., Martínez Pillet, V., Ruiz Cobo, B., del Toro Iniesta, J. C., & Vázquez, M. 1994, A&A, 291, 622
Frutiger, C. 2000, Ph.D. Thesis, Institute of Astronomy, ETH, Zürich, No. 13896
Jun, B., Norman, M. L., & Stone, J. 1995, ApJ, 453, 332
Kippenhahn, R., & Möllenhoff, C. 1975, Elementare Plasmaphysik (Zürich: Wissenschaftsverlag)
Langhans, K., Scharmer, G., Kiselman, D., & Löfdahl, M. G. 2007, A&A, 464, 763
Mathew, S. K., Lagg, A., Solanki, S. K., et al. 2003, A&A, 410, 695
Montesinos, B., & Thomas, J. 1997, Nature, 390, 485
Müller, D. A. N., Schlichenmaier, R., Steiner, O., & Stix, M. 2002, A&A, 393, 305
Müller, D. A. N, Schlichenmaier, R., Fritz, G., & Beck, C. 2006, A&A, 460, 925
Rimmele, T., & Marino, J. 2006, ApJ, 646, 593
Rouppe van der Voort, L., Löfdahl, M. G., Kiselman, D., & Scharmer, G. B. 2004, A&A, 414, 717
Rüedi, I., Solanki, S. K., Keller, C. U., & Frutiger, C. 1998, A&A, 338, 1089
Rüedi, I., Solanki, S. K., & Keller, C. U. 1999, A&A, 348, L37
Sánchez Almeida, J., & Lites, B. 1992, ApJ, 398, 359
Scharmer, G., & Spruit, H. 2006, A&A, 460, 605
Scharmer, G., Gudiksen , B. V., Kiselman, D., et al. 2002, Nature, 420, 151
Schlichenmaier, R., Jahn, K., & Schmidt, H. U. 1998, A&A, 337, 897
Schlichenmaier, R., Müller, D. A. N., Steiner, O., & Stix, M. 2002, A&A, 381, L77
Schlichenmaier, R., Bellot Rubio, L. R., & Tritschler, A. 2004, A&A, 415, 731
Schüssler, M., & Vögler, A. 2006, ApJ, 641, L73
Spruit, H. C., & Scharmer, G. B. 2006, A&A, 447, 343
Solanki, S. K. 2003, A&ARv, 11, 153
Solanki, S. K., & Montavon, C. A. P. 1993, A&A, 275, 283
Sütterlin, P., Bellot Rubio, L. R., & Schlichenmaier, R. 2004, A&A, 424, 1049
Thomas, J., & Weiss, N. 2004, ARA&A, 42, 517
del Toro Iniesta, J. C., Tarbell, T. D., & Ruiz Cobo, B. 1994, ApJ, 436, 400
del Toro Iniesta, J. C., Bellot Rubio, L. R., & Collados, M. 2001, ApJ, 549, L139
Westendorp Plaza, C., del Toro Iniesta, J. C., Ruiz Cobo, B., et al. 1997, Nature, 389, 47